Composite Structures 98 (2013) 160–168

Contents lists available at SciVerse ScienceDirect

Composite Structures

journal homepage: www.elsevier.com/locate/compstruct

Buckling analysis of functionally graded carbon nanotube-reinforced composite plates using the element-free *kp*-Ritz method

Z.X. Lei [a,b,c], K.M. Liew [a,c,*], J.L. Yu [b,c]

[a] Department of Civil and Architectural Engineering, City University of Hong Kong, Kowloon, Hong Kong
[b] CAS Key Laboratory of Mechanical Behavior and Design of Materials, University of Science and Technology of China, PR China
[c] USTC-CityU Joint Advanced Research Centre, Suzhou, PR China

ARTICLE INFO

Article history:
Available online 29 November 2012

Keywords:
Buckling
Carbon nanotube
Composite plate
First-order shear deformation plate theory
Mesh-free method

ABSTRACT

This paper presents the buckling analysis of functionally graded carbon nanotube-reinforced composite (FG-CNTRC) plates under various in-plane mechanical loads, using the element-free *kp*-Ritz method. The first-order shear deformation plate theory is applied and a set of mesh-free kernel particle functions are used to approximate two-dimensional displacement fields. Effective properties of materials of the plates reinforced by single-walled carbon nanotubes (SWCNTs) are estimated through a micromechanical model based on either the Eshelby–Mori–Tanaka approach or the extended rule of mixture. Comparison study and numerical simulations with various parameters are conducted to assess efficacy and accuracy of the present method for analysis of buckling of SWCNT-reinforced composite plates. Results demonstrate that the change of carbon nanotube volume fraction, plate width-to-thickness ratio, plate aspect ratio, loading condition and temperature have pronounced effects on buckling strength of CNTRC plates as well as the boundary condition.

1. Introduction

Recently, carbon nanotubes (CNTs), as a new type of advanced materials, have attracted a great deal of interest of researchers. Due to their extremely attractive mechanical, electrical and thermal properties, CNTs have promising applications in polymer composites as a potential reinforcement and multi-functional element [1,2]. Therefore, the introduction of CNTs into a polymer matrix may greatly improve mechanical properties of the resulting nanocomposites, such as tensile strength and elastic modulus [3].

Most investigations of carbon nanotubes-reinforced composites (CNTRCs) have focused on material properties and researchers have discovered that mechanical, electrical and thermal properties of polymer composites can be considerably improved by adding small amounts of CNTs. Odegard et al. [4] presented a constitutive modeling of nanotubes-reinforced polymer composites with nanotubes/polymer interface modeled as an effective continuum fiber by using an equivalent-continuum model. Gary et al. [5] obtained the effective elastic properties of CNTRCs through a variety of micromechanics techniques with the effective properties of CNTs calculated utilizing a composite cylinders micromechanics technique as a first step in a two-step process. Fidelus et al. [6] examined the thermo-mechanical properties of epoxy-based nanocomposites based on low weight fractions of randomly oriented single- and multi-walled carbon nanotubes. Han and Elliot [7] presented classical molecular dynamics (MD) simulations of model polymer/CNT composites constructed by embedding a single wall (10, 10) CNT into two different amorphous polymer matrices. By using MD method, the stress–strain behavior of carbon nanotube-reinforced Epon862 composites was also studied by Zhu et al. [8].

Although these studies are quite useful, the ultimate purpose of development of this advanced material is to explore potential applications of CNTRCs in actual structures, such as CNT-reinforced beams, plates or shells. Wuite and Adali [9] studied deflection and stress behaviors of nanocomposite reinforced beams using a multiscale analysis. Their results showed that reinforcement by adding a small proportion of nanotube leads to significant improvement in beam stiffness. Vodenitcharova and Zhang [10] presented analyses of pure bending and bending-induced local buckling of a nanocomposite beam based on a continuum mechanical model and found that single-walled carbon nanotube (SWCNT) buckles at smaller bending angles and greater flattening ratios in thicker matrix layers. Formica et al. [11] investigated vibration behaviors of CNTRC plates by employing an equivalent continuum model based on the Eshelby–Mori–Tanaka approach. Based on the classical laminated plate theory and third-order shear deformation theory, Arani et al. [12] analytically and numerically studied buckling behaviors of laminated composite plates. The optimal orientation of CNTs to achieve the highest critical load and corresponding mode shape

* Corresponding author at: Department of Civil and Architectural Engineering, City University of Hong Kong, Kowloon, Hong Kong.
E-mail address: kmliew@cityu.edu.hk (K.M. Liew).

0263-8223/$ - see front matter © 2012 Elsevier Ltd. All rights reserved.
http://dx.doi.org/10.1016/j.compstruct.2012.11.006

were calculated for different kinds of boundary conditions as well as aspect ratios of the plates. Shen [13,14] presented a postbuckling analysis of cylindrical shells reinforced by SWCNTs subjected to axial compression and lateral or hydrostatic pressure in thermal environments. Results revealed that the mid-plane symmetric functionally graded distribution of reinforcements can increase the buckling load as well as postbuckling strength of the shells. They also confirmed that the postbuckling equilibrium path for both FG- and UD-CNTRC cylindrical shells under axial compression is unstable.

In traditional nanocomposites, the resulting mechanical, thermal, or physical properties do not vary spatially at the macroscopic level since nanotubes distribute either uniformly or randomly in the composites. Stimulated by the concept of functionally graded materials (FGMs) with properties that vary spatially according to a certain non-uniform distribution of the reinforcement phase, Shen [15] presented a non-linear bending analysis of functionally graded carbon nanotube-reinforced composite (FG-CNTRC) plates in thermal environments using a two-step perturbation technique. The results showed that non-linear bending behaviors of CNTRC plate can be considerably improved as CNTs distribute functionally in the matrix. By using the finite element method (FEM), analyses of bending and free vibration were carried out for various types of functionally graded CNTRC plates by Zhu et al. [16]. They discovered that CNT reinforcements distributed close to top and bottom are more efficient than those distributed near the mid-plane for increasing the stiffness of CNTRC plates. Based on the Timoshenko beam theory, non-linear free vibrations of functionally graded CNTRC beams were analyzed with the Ritz method and direct iterative technique by Ke et al. [17]. They found linear and non-linear frequencies of FG-CNTRC beam with symmetrical distribution of CNTs higher than those of beams with uniform or asymmetrical distribution of CNTs. For improving buckling and postbuckling behaviors of CNTRC structures, Shen and Zhang [18] investigated thermal buckling and postbuckling behaviors of FG-CNTRC plates and found that CNTRC plate with intermediate nanotube volume fraction does not have intermediate buckling temperature and initial thermal postbuckling strength.

In the present work, a buckling analysis of FG-CNTRC plates under different in-plane loading conditions in thermal environment is presented using the element-free *kp*-Ritz method, which has already been successfully applied in many fields [19–22]. Two kinds of CNTRC plates, namely, uniformly distributed (UD) and functionally graded (FG) CNTRC plates, are considered. The eigenvalue equations of buckling analysis of CNTRC plates are obtained by applying the Ritz procedure to the energy function of the system. In order to improve computational efficiency and avoid shear locking for very thin plates, a stabilized conforming nodal integration approach is used to calculate the plate bending stiffness, and the shear and membrane terms are evaluated using a direct nodal integration method. Effects of CNT volume fraction, plate width-to-thickness ratio, plate aspect ratio, boundary condition, in-plane loading condition and temperature change on buckling strength of CNTRC plates are examined in detail.

2. Carbon nanotube-reinforced composites

Three types of distributions of CNTs in CNTRC plates with length a, width b and thickness h are considered (Fig. 1). UD denotes the uniform distribution and the other two types of functionally graded distributions of CNTs are represented by FG-O and FG-X. The plates are assumed to be made of a mixture of SWCNTs and the matrix. The matrix is assumed to be isotropic and material properties of SWCNTs are chirality-, size- and temperature-dependent [23–26]. Distributions of CNTs along the thickness direction of UD- and the other two types FG- of CNTRC plates are assumed to be as follows:

$$V_{CNT}(z) = \begin{cases} V^*_{CNT} & (\text{UD} \quad \text{CNTRC}), \\ 2\left(1 - \frac{2|z|}{h}\right)V^*_{CNT} & (\text{FG-O} \quad \text{CNTRC}), \\ 2\left(\frac{2|z|}{h}\right)V^*_{CNT} & (\text{FG-X} \quad \text{CNTRC}), \end{cases} \tag{1}$$

where

$$V^*_{CNT} = \frac{w_{CNT}}{w_{CNT} + (\rho^{CNT}/\rho^m) - (\rho^{CNT}/\rho^m)w_{CNT}}, \tag{2}$$

where w_{CNT} is the fraction of mass of CNTs and ρ^m and ρ^{CNT} are densities of the matrix and CNTs, respectively. V_{CNT} and V^*_{CNT} are the CNT volume fractions of FG- and UD-CNTRCs and we assume $V_{CNT} = V^*_{CNT}$, that means UD-CNTRC plate and the other two types of FG-CNTRC plates have the same mass volume of CNTs.

As the load transfer between the nanotube and matrix is less than perfect, several micromechanical models have been

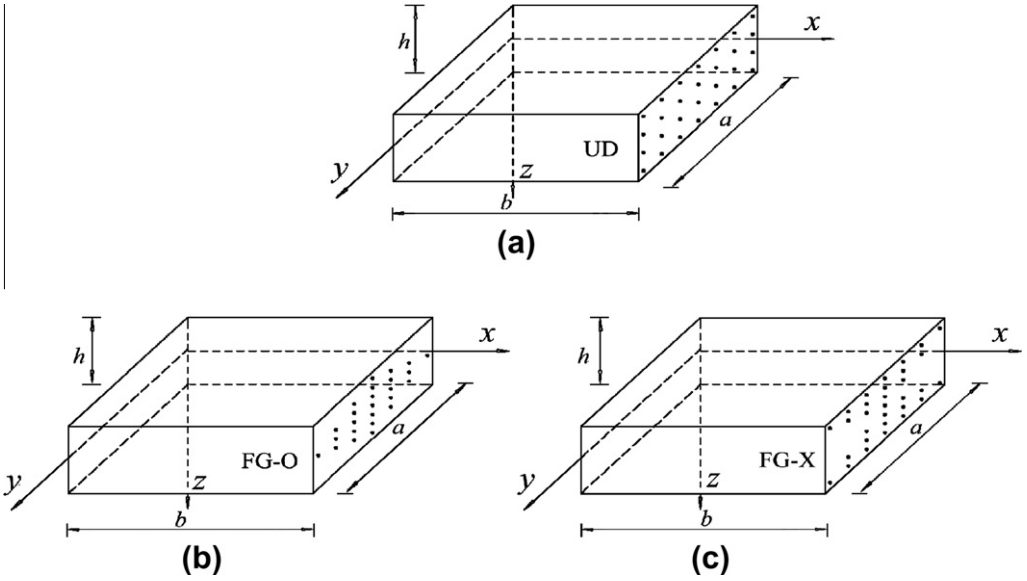

Fig. 1. Configurations of carbon nanotube reinforced composite plates. (a) UD CNTRC plate; (b) FG-O CNTRC plate; (c) FG-X CNTRC plate.

developed to predict properties of CNT-reinforced nanocomposites, e.g. Mori–Tanaka scheme [27,28] and the rule of mixture [1,6]. A synergism between the Mori–Tanaka scheme and the rule of mixture for functionally graded ceramic–metal beams was reported in [29] and a comparison study between Eshelby–Mori–Tanaka scheme and the extended rule of mixture was also conducted for the vibration analysis of continuously graded carbon nanotubes-reinforced cylindrical panels in [30].

2.1. Eshelby–Mori–Tanaka approach

The proposed model is framed within the Eshelby for elastic inclusions. Since the original theory of Eshelby [31,32] is restricted to one single inclusion in a semi-infinite elastic, homogeneous and isotropic medium, the theory, generalized by Mori–Tanaka [33], allows to extend the original approach to the practical case of multiple inhomogeneities embedded into a finite domain. The Eshelby–Mori–Tanaka approach, known as the equivalent inclusion-average stress method, is based on the equivalent elastic inclusion idea of Eshelby and the concept of average stress in the matrix due to Mori–Tanaka. According to Benveniste's revision [34], effective elastic moduli tensor $\mathbf{C}$ of CNTRCs is expressed as

$$\mathbf{C} = \mathbf{C}_m + V_{CNT}\langle(\mathbf{C}_{CNT} - \mathbf{C}_m)\cdot\mathbf{A}\rangle\cdot[V_m\mathbf{I} + V_{CNT}\langle\mathbf{A}\rangle]^{-1}, \tag{3}$$

where $\mathbf{C}_m$ and $\mathbf{C}_{CNT}$ are the stiffness tensors of the matrix and CNT, respectively and $\mathbf{I}$ is the fourth-order unit tensor. It should be note that the brackets represent an average overall possible orientation of the inclusions. $\mathbf{A}$ is the dilute mechanical strain concentration tensor, and is given by

$$\mathbf{A} = \left[\mathbf{I} + \mathbf{S}\cdot\mathbf{C}_m^{-1}\cdot(\mathbf{C}_{CNT} - \mathbf{C}_m)\right]^{-1}, \tag{4}$$

where $\mathbf{S}$ is the fourth-order Eshelby tensor [31] that is specialized to the case of cylindrical inclusions representative of the CNTs and depends on their orientation by Mura [35].

2.2. Extended rule of mixture

According to the extended rule of mixture, effective material properties of CNTRC plates can be expressed as [15]:

$$E_{11} = \eta_1 V_{CNT} E_{11}^{CNT} + V_m E^m, \tag{5}$$

$$\frac{\eta_2}{E_{22}} = \frac{V_{CNT}}{E_{22}^{CNT}} + \frac{V_m}{E^m}, \tag{6}$$

$$\frac{\eta_3}{G_{12}} = \frac{V_{CNT}}{G_{12}^{CNT}} + \frac{V_m}{G^m}, \tag{7}$$

where E_{11}^{CNT} and E_{22}^{CNT} are Young's moduli of CNTs in longitudinal and transverse directions, respectively. G_{12}^{CNT} is the shear modulus of CNTs. E^m and G^m are Young's modulus and shear modulus of the isotropic matrix. CNT efficiency parameters η_j ($j = 1, 2, 3$) are introduced into Eqs. (1)–(3) to account load transfer between the nanotubes and polymeric phases (e.g. the surface effect, strain gradient effect, and intermolecular coupling effect) and other effects on the effective material properties of CNTRCs. Shen [15] determined the CNT efficiency parameter by matching Young's moduli E_{11} and E_{22} of CNTRCs obtained by the rule of mixture to MD results of Han and Elliott [7]. V_{CNT} and V_m are CNT and matrix volume fractions and have the relationship:

$$V_{CNT} + V_m = 1. \tag{8}$$

As Poisson's ratio depends weakly on position, we assume υ_{12} to be constant through the thickness of CNTRC plates as follows:

$$\upsilon_{12} = V_{CNT}^{*}\upsilon_{12}^{CNT} + V_m\upsilon^m, \tag{9}$$

where υ_{12}^{CNT} and υ^m are Poisson's ratios of CNTs and the matrix, respectively.

Similarly, thermal expansion coefficients can be calculated by

$$\alpha_{11} = V_{CNT}\alpha_{11}^{CNT} + V_m\alpha^m, \tag{10}$$

$$\alpha_{22} = (1+\upsilon_{12}^{CNT})V_{CNT}\alpha_{22}^{CNT} + (1+\upsilon^m)V_m\alpha^m - \upsilon_{12}\alpha_{11}, \tag{11}$$

where α_{11}^{CNT} and α_{22}^{CNT} are thermal expansion coefficients of CNTs in longitudinal and transverse directions, respectively. α^m is the expansion coefficient of the matrix.

3. Theoretical formulations

3.1. Total potential energy functional

Formulations of buckling of CNTRC plates are derived from the Ritz method based on the first-order shear deformation theory (FSDT) [36]. The displacement field can be expressed as

$$u(x,y,z) = u_0(x,y) + z\phi_x(x,y), \tag{12}$$

$$v(x,y,z) = v_0(x,y) + z\phi_y(x,y), \tag{13}$$

$$w(x,y,z) = w_0(x,y), \tag{14}$$

where (u, v, w) are the displacements of a generic point (x, y, z) in the CNTRC plate, (u_0, v_0, w_0) represent the displacements of a point at the mid-plane of the plate and (ϕ_x, ϕ_y) denote rotations of a transverse normal about positive y and negative x axes, respectively. The strain components at a genetic point of the plate are given by

$$\begin{Bmatrix}\varepsilon_{xx}\\ \varepsilon_{yy}\\ \gamma_{xy}\end{Bmatrix} = \boldsymbol{\varepsilon}_0 + z\boldsymbol{\kappa}, \quad \begin{Bmatrix}\gamma_{yz}\\ \gamma_{xz}\end{Bmatrix} = \boldsymbol{\gamma}_0, \tag{15}$$

where

$$\boldsymbol{\varepsilon}_0 = \begin{Bmatrix}\frac{\partial u_0}{\partial x}\\ \frac{\partial v_0}{\partial y}\\ \frac{\partial u_0}{\partial y} + \frac{\partial v_0}{\partial x}\end{Bmatrix}, \quad \boldsymbol{\kappa} = \begin{Bmatrix}\frac{\partial \phi_x}{\partial x}\\ \frac{\partial \phi_y}{\partial y}\\ \frac{\partial \phi_x}{\partial y} + \frac{\partial \phi_y}{\partial x}\end{Bmatrix}, \quad \boldsymbol{\gamma}_0 = \begin{Bmatrix}\phi_y + \frac{\partial w_0}{\partial y}\\ \phi_x + \frac{\partial w_0}{\partial x}\end{Bmatrix}. \tag{16}$$

Then, the constitutive relations are expressed as

$$\begin{Bmatrix}\sigma_{xx}\\ \sigma_{yy}\\ \sigma_{xy}\\ \sigma_{yz}\\ \sigma_{xz}\end{Bmatrix} = \begin{bmatrix}Q_{11} & Q_{12} & 0 & 0 & 0\\ Q_{12} & Q_{22} & 0 & 0 & 0\\ 0 & 0 & Q_{66} & 0 & 0\\ 0 & 0 & 0 & Q_{44} & 0\\ 0 & 0 & 0 & 0 & Q_{55}\end{bmatrix}\left(\begin{Bmatrix}\varepsilon_{xx}\\ \varepsilon_{yy}\\ \gamma_{xy}\\ \gamma_{yz}\\ \gamma_{xz}\end{Bmatrix} - \begin{Bmatrix}\alpha_{11}\\ \alpha_{22}\\ 0\\ 0\\ 0\end{Bmatrix}\Delta T\right), \tag{17}$$

where

$$Q_{11} = \frac{E_{11}}{1-\upsilon_{12}\upsilon_{21}}, \quad Q_{22} = \frac{E_{22}}{1-\upsilon_{12}\upsilon_{21}}, \quad Q_{12} = \frac{\upsilon_{21}E_{11}}{1-\upsilon_{12}\upsilon_{21}}, \tag{18}$$

$$Q_{66} = G_{12}, \quad Q_{44} = G_{23}, \quad Q_{55} = G_{13}, \tag{19}$$

and ΔT is the temperature change with respect to a reference state. E_{11} and E_{22} are effective Young's moduli of CNTRC plates in the principal material coordinates, G_{12}, G_{13} and G_{23} are the shear moduli, υ_{12} and υ_{21} are Poisson's ratios and α_{11} and α_{22} are thermal expansion coefficients.

With usual assumptions of FSDT, the relation between the stress resultants and the strains can be written as

$$\begin{Bmatrix}\mathbf{N}\\ \mathbf{M}\\ \mathbf{Qs}\end{Bmatrix} = \begin{bmatrix}\mathbf{A} & \overline{\mathbf{B}} & 0\\ \overline{\mathbf{B}} & \mathbf{D} & 0\\ 0 & 0 & \mathbf{A}^s\end{bmatrix}\begin{Bmatrix}\boldsymbol{\varepsilon}_0\\ \boldsymbol{\kappa}\\ \boldsymbol{\gamma}_0\end{Bmatrix} - \begin{Bmatrix}\mathbf{N}^{\mathrm{T}}\\ \mathbf{M}^{\mathrm{T}}\\ 0\end{Bmatrix}, \tag{20}$$

where the in-plane force resultants, moment resultants, transverse force resultants and thermal stress resultants are defined as

$$\mathbf{N}=\begin{Bmatrix}N_{xx}\\N_{yy}\\N_{xy}\end{Bmatrix}=\int_{-h/2}^{h/2}\begin{Bmatrix}\sigma_{xx}\\\sigma_{yy}\\\sigma_{xy}\end{Bmatrix}dz,$$
$$\mathbf{M}=\begin{Bmatrix}M_{xx}\\M_{yy}\\M_{xy}\end{Bmatrix}=\int_{-h/2}^{h/2}\begin{Bmatrix}\sigma_{xx}\\\sigma_{yy}\\\sigma_{xy}\end{Bmatrix}zdz,$$
$$\mathbf{Qs}=\begin{Bmatrix}Q_y\\Q_x\end{Bmatrix}=\int_{-h/2}^{h/2}\begin{Bmatrix}\sigma_{yz}\\\sigma_{xz}\end{Bmatrix}dz, \tag{21}$$

$$\mathbf{N}^T=\int_{-h/2}^{h/2}[\,\alpha_{11}\quad\alpha_{22}\quad 0\,](Q_{11}+Q_{12})\Delta T dz,$$
$$\mathbf{M}^T=\int_{-h/2}^{h/2}[\,\alpha_{11}\quad\alpha_{22}\quad 0\,](Q_{11}+Q_{12})\Delta T z dz. \tag{22}$$

The extensional **A**, coupling $\overline{\mathbf{B}}$, bending **D** and transverse shear $\mathbf{A}^s$ stiffness are given by

$$(A_{ij},B_{ij},D_{ij})=\int_{-h/2}^{h/2}Q_{ij}(1,z,z^2)dz,\quad A_{ij}^s=K\int_{-h/2}^{h/2}Q_{ij}dz, \tag{23}$$

where A_{ij}, B_{ij} and D_{ij} are defined for i,j = 1, 2, 6 and i,j = 4, 5 in A_{ij}^s. K denotes the transverse shear correction coefficient and is suggested to be $K = 5/(6-(v_1V_1+v_2V_2))$ for functionally graded materials by Efraim and Eisenberger [37].

Strain energy of the CNTRC plate is expressed as

$$U_\varepsilon=\frac{1}{2}\int_\Omega \boldsymbol{\varepsilon}^{\mathrm{T}}\mathbf{S}\boldsymbol{\varepsilon}d\Omega, \tag{24}$$

where

$$\boldsymbol{\varepsilon}=\begin{Bmatrix}\boldsymbol{\varepsilon}_0\\\boldsymbol{\kappa}\\\gamma_0\end{Bmatrix},\quad \mathbf{S}=\begin{bmatrix}\mathbf{A}&\overline{\mathbf{B}}&\mathbf{0}\\\overline{\mathbf{B}}&\mathbf{D}&\mathbf{0}\\\mathbf{0}&\mathbf{0}&\mathbf{A}^s\end{bmatrix}. \tag{25}$$

The potential energy due to in-plane loading is given by

$$W_g=\int_\Omega\begin{bmatrix}\frac{\partial w}{\partial x}&\frac{\partial w}{\partial y}\end{bmatrix}\begin{bmatrix}\gamma_1N_x^0&0\\0&\gamma_2N_y^0\end{bmatrix}\begin{bmatrix}\frac{\partial w}{\partial x}\\\frac{\partial w}{\partial y}\end{bmatrix}d\Omega, \tag{26}$$

Thus the total potential energy function of the plate can be expressed as

$$\Pi_s=U_\varepsilon-W_g. \tag{27}$$

3.2. Discrete system equations

Based on the kernel particle Ritz method, for a plate discretized by a set of nodes $\boldsymbol{x}_I$, I = 1, …, NP, the displacement field can be expressed as

$$u^h=\sum_{I=1}^{NP}\psi_I(x)\boldsymbol{u}_I, \tag{28}$$

where $\psi_I(\boldsymbol{x})$ and $\boldsymbol{u}_I$ are the shape function and nodal parameter associated with node I, respectively.

The shape function is expressed as

$$\psi_I(\boldsymbol{x})=C(\boldsymbol{x};\boldsymbol{x}-\boldsymbol{x}_I)\Phi_a(\boldsymbol{x}-\boldsymbol{x}_I), \tag{29}$$

where $\Phi_a(\boldsymbol{x}-\boldsymbol{x}_I)$ is the kernel function, and $C(\boldsymbol{x};\boldsymbol{x}-\boldsymbol{x}_I)$ is the correction function which can be expressed by a linear combination of polynomial basis functions, as follows:

$$C(\boldsymbol{x};\boldsymbol{x}-\boldsymbol{x}_I)=\mathbf{H}^{\mathrm{T}}(\boldsymbol{x}-\boldsymbol{x}_I)\mathbf{b}(\boldsymbol{x}), \tag{30}$$

where

$$\mathbf{b}(x)=[b_0(x,y),b_1(x,y),b_2(x,y),b_3(x,y),b_4(x,y),b_5(x,y)]^{\mathrm{T}}, \tag{31}$$

$$\mathbf{H}^{\mathrm{T}}(\boldsymbol{x}-\boldsymbol{x}_I)=[1,x-x_I,y-y_I,(x-x_I)(y-y_I),(x-x_I)^2,(y-y_I)^2], \tag{32}$$

where **H** is a vector of the quadratic basis and $\mathbf{b}(\boldsymbol{x})$ is a coefficient function of x and y, to be determined. Then, the shape function can be written as

$$\psi_I(\boldsymbol{x})=\mathbf{b}^{\mathrm{T}}(\boldsymbol{x})\mathbf{H}(\boldsymbol{x}-\boldsymbol{x}_I)\Phi_a(\boldsymbol{x}-\boldsymbol{x}_I), \tag{33}$$

Substituting Eq. (33) into reproduction condition leads to

$$\sum_{I=1}^{NP}\psi_I(\boldsymbol{x})x_I^py_I^q=x^py^q\quad\text{for } p+q=0,1,2. \tag{34}$$

We can obtain coefficient $\mathbf{b}(\boldsymbol{x})$ as

$$\mathbf{b}(\boldsymbol{x})=\mathbf{M}^{-1}(\boldsymbol{x})\mathbf{H}(\mathbf{0}), \tag{35}$$

where

$$\mathbf{M}(\boldsymbol{x})=\sum_{I=1}^{NP}\mathbf{H}(\boldsymbol{x}-\boldsymbol{x}_I)\mathbf{H}^{\mathrm{T}}(\boldsymbol{x}-\boldsymbol{x}_I)\Phi_a(\boldsymbol{x}-\boldsymbol{x}_I), \tag{36}$$
$$\mathbf{H}(\mathbf{0})=[1,0,0,0,0,0,]^{\mathrm{T}}, \tag{37}$$

For two-dimensional plate problem, the kernel function $\Phi_a(\boldsymbol{x}-\boldsymbol{x}_I)$ is defined as

$$\Phi_a(\boldsymbol{x}-\boldsymbol{x}_I)=\Phi_a(x)\cdot\Phi_a(y), \tag{38}$$

where

$$\Phi_a(x)=\varphi\left(\frac{x-x_I}{a}\right). \tag{39}$$

The cubic spline function is chosen as the weight function $\varphi(x)$, and is given by

$$\varphi_z(z_I)=\begin{Bmatrix}\frac{2}{3}-4z_I^2+4z_I^3 & \text{for } 0\leqslant|z_I|\leqslant\frac{1}{2}\\\frac{4}{3}-4z_I+4z_I^2-\frac{4}{3}z_I^3 & \text{for } \frac{1}{2}<|z_I|\leqslant 1\\0 & \text{otherwise}\end{Bmatrix}, \tag{40}$$

where $z_I=\frac{x-x_I}{d_I}$ and d_I is the size of the support of node I, calculated by

$$d_I=d_{\max}c_I, \tag{41}$$

where distance c_I is chosen by searching for a sufficient number of nodes to avoid the singularity of matrix **M** and $d_{\max}$ is a scaling factor ranging from 2.0 to 4.0.

The shape function can be expressed as

$$\psi_I(\boldsymbol{x})=\mathbf{H}^{\mathrm{T}}(\mathbf{0})\mathbf{M}^{-1}(\boldsymbol{x})\mathbf{H}(\boldsymbol{x}-\boldsymbol{x}_I)\Phi_a(\boldsymbol{x}-\boldsymbol{x}_I). \tag{42}$$

As the shape function does not have Kronecker delta property, the essential boundary conditions cannot be directly imposed. The transformation method [38] is employed to enforce the essential boundary conditions in this paper.

Substituting Eq. (28) into Eq. (27) and performing the Ritz minimization procedure, we can obtain eigenvalue equations of plate buckling, as follows:

$$(\mathbf{K}+\lambda\mathbf{K}_g)\mathbf{u}=\mathbf{0}. \tag{43}$$

where λ is the critical buckling load of CNTRC plates and **K** and $\mathbf{K}_g$ represent the linear stiffness matrix and geometric stiffness matrix, respectively, and are given by

$$\mathbf{K} = \mathbf{K}^b + \mathbf{K}^m + \mathbf{K}^s, \tag{44}$$

$$\mathbf{K}_{IJ}^b = \int_\Omega \mathbf{B}_I^{b^T} \mathbf{D} \mathbf{B}_J^b d\Omega, \tag{45}$$

$$\mathbf{K}_{IJ}^m = \int_\Omega \mathbf{B}_I^{m^T} \mathbf{A} \mathbf{B}_J^m d\Omega + \int_\Omega \mathbf{B}_I^{m^T} \overline{\mathbf{B}} \mathbf{B}_J^b d\Omega + \int_\Omega \mathbf{B}_I^{b^T} \overline{\mathbf{B}} \mathbf{B}_J^m d\Omega, \tag{46}$$

$$\mathbf{K}_{IJ}^s = \int_\Omega \mathbf{B}_I^{s^T} \mathbf{A}^s \mathbf{B}_J^s d\Omega, \tag{47}$$

$$\mathbf{K}_g = \int_\Omega \overline{\mathbf{G}}_I^T \overline{\mathbf{N}} \overline{\mathbf{G}}_J d\Omega. \tag{48}$$

Stiffness matrices in Eqs. (45)–(48) are evaluated via the stabilized nodal integration [39] and direct nodal integration (instead of Gauss integration) commonly used in mesh-free methods. Compared with Gauss integration, the stabilized nodal integration and direct nodal integration may reduce the high computational cost and eliminate the errors caused by the mismatch between quadrature cells and shape function supports [40]. Approximations of Eqs. (45)–(48) are given as follows:

$$\mathbf{K}_{IJ}^b = \sum_{L=1}^{NP} \widetilde{\mathbf{B}}_I^{b^T}(\mathbf{x}_L) \mathbf{D} \widetilde{\mathbf{B}}_J^b(\mathbf{x}_L) A_L, \tag{49}$$

$$\mathbf{K}_{IJ}^m = \sum_{L=1}^{NP} \left[\mathbf{B}_I^{m^T}(\mathbf{x}_L) \mathbf{A} \mathbf{B}_J^m(\mathbf{x}_L) + \mathbf{B}_I^{m^T}(\mathbf{x}_L) \overline{\mathbf{B}} \mathbf{B}_J^b(\mathbf{x}_L) + \mathbf{B}_I^{b^T}(\mathbf{x}_L) \overline{\mathbf{B}} \mathbf{B}_J^m(\mathbf{x}_L) \right] A_L, \tag{50}$$

$$\mathbf{K}_{IJ}^s = \sum_{L=1}^{NP} \mathbf{B}_I^{s^T}(\mathbf{x}_L) \mathbf{A}^s \mathbf{B}_J^s(\mathbf{x}_L) A_L, \tag{51}$$

$$\mathbf{K}^g = \sum_{L=1}^{NP} \overline{\mathbf{G}}_I^T(\mathbf{x}_L) \overline{\mathbf{N}} \overline{\mathbf{G}}_J(\mathbf{x}_L) A_L, \tag{52}$$

where $\mathbf{x}_L$ and A_L denote the node coordinate and nodal representative area, respectively. Matrices $\widetilde{\mathbf{B}}_I^b(\mathbf{x}_L)$, $\mathbf{B}_I^b(\mathbf{x}_L)$, $\mathbf{B}_I^m(\mathbf{x}_L)$, $\mathbf{B}_I^s(\mathbf{x}_L)$, $\overline{\mathbf{G}}(\mathbf{x}_L)$ and $\overline{\mathbf{N}}$ are calculated by

$$\widetilde{\mathbf{B}}_I^b(\mathbf{x}_L) = \begin{bmatrix} 0 & 0 & 0 & \tilde{b}_{Ix}(\mathbf{x}_L) & 0 \\ 0 & 0 & 0 & 0 & \tilde{b}_{Iy}(\mathbf{x}_L) \\ 0 & 0 & 0 & \tilde{b}_{Iy}(\mathbf{x}_L) & \tilde{b}_{Ix}(x_L) \end{bmatrix}, \tag{53}$$

$$\tilde{b}_{Ix}(\mathbf{x}_L) = \frac{1}{A_L} \int_{\Gamma_L} \psi_I(\mathbf{x}_L) n_x(\mathbf{x}_L) d\Gamma, \quad \tilde{b}_{Iy}(\mathbf{x}_L) = \frac{1}{A_L} \int_{\Gamma_L} \psi_I(\mathbf{x}_L) n_y(\mathbf{x}_L) d\Gamma, \tag{54}$$

$$\mathbf{B}_I^b(\mathbf{x}_L) = \begin{bmatrix} 0 & 0 & 0 & \frac{\partial \psi_I(\mathbf{x}_L)}{\partial x} & 0 \\ 0 & 0 & 0 & 0 & \frac{\partial \psi_I(\mathbf{x}_L)}{\partial y} \\ 0 & 0 & 0 & \frac{\partial \psi_I(\mathbf{x}_L)}{\partial y} & \frac{\partial \psi_I(\mathbf{x}_L)}{\partial x} \end{bmatrix},$$

$$\mathbf{B}_I^m(\mathbf{x}_L) = \begin{bmatrix} \frac{\partial \psi_I(\mathbf{x}_L)}{\partial x} & 0 & 0 & 0 & 0 \\ 0 & \frac{\partial \psi_I(\mathbf{x}_L)}{\partial y} & 0 & 0 & 0 \\ \frac{\partial \psi_I(\mathbf{x}_L)}{\partial y} & \frac{\partial \psi_I(\mathbf{x}_L)}{\partial x} & 0 & 0 & 0 \end{bmatrix}, \tag{55}$$

$$\mathbf{B}_I^s(\mathbf{x}_L) = \begin{bmatrix} 0 & 0 & \frac{\partial \psi_I(\mathbf{x}_L)}{\partial x} & \psi_I(\mathbf{x}_L) & 0 \\ 0 & 0 & \frac{\partial \psi_I(\mathbf{x}_L)}{\partial y} & 0 & \psi_I(\mathbf{x}_L) \end{bmatrix}, \tag{56}$$

$$\overline{\mathbf{G}}(\mathbf{x}_L) = \begin{bmatrix} 0 & 0 & \frac{\partial \psi_I(\mathbf{x}_L)}{\partial x} & 0 & 0 \\ 0 & 0 & \frac{\partial \psi_I(\mathbf{x}_L)}{\partial y} & 0 & 0 \end{bmatrix}, \quad \overline{\mathbf{N}} = \begin{bmatrix} \gamma_1 \overline{N}_{xx} & 0 \\ 0 & \gamma_2 \overline{N}_{yy} \end{bmatrix}. \tag{57}$$

4. Numerical results

In this section, several numerical examples are presented to study buckling behaviors of CNTRC plates under various in-plane mechanical loading conditions in thermal environment. Poly{(m-phenylenevinylene)-co-[(2,5-dioctoxy-p-phenylene) vinylene]}, referred as PmPV, is selected as the matrix, material properties of which are assumed to be $\nu^m = 0.34$, $\alpha^m = 45(1 + 0.0005\Delta T) \times 10^{-6}$ K and $E^m = (3.51 - 0.0047T)$ GPa, where $T = T_0 + \Delta T$ and $T_0 = 300$ K (room temperature). For the Eshelby–Mori–Tanaka approach, the representative values of the properties of SWCNTs are taken from the analytical results of Popov et al. [41], while for the extended rule of mixture, properties of SWCNTs are obtained from MD simulation results reported by Zhang and Shen [10]. Unless otherwise specified, the Eshelby–Mori–Tanaka approach is applied to predict effective material properties of CNTRCs. The shape function of two-dimensional displacement approximations is constructed with the kernel particle function, and a scaling factor of 3.2, that represents the size of the support, is used for all cases in this paper. A regular nodal distribution 21×21 is chosen following convergence studies.

4.1. Comparison study

To verify the present formulation, a comparison is carried out for simply supported isotropic plate under uniaxial compressive pressure ($\gamma_1 = -1$, $\gamma_2 = 0$). Geometric properties of this plate are $a = b = 10$ in., $h = 0.2$ in., and its material properties are Young's modulus $E = 3.0 \times 10^6$ psi and Poisson ratio $\nu = 0.3$. A convergence study in terms of number of nodes is carried out to verify the accuracy and efficiency of the present method. Buckling load parameters $\overline{N}_{cr} = N_{cr} a^2 / D_0 (D_0 = Eh^3/12(1-\nu^2))$ for the first four modes are listed in Table 2 and analytical solutions given by Timoshenko and Geer [42] are also provided for comparison. It can be found that the present results agree well with analytical solutions for all modes.

4.2. Parameter studies

In this section, detailed case studies are carried out to investigate effects of plate width-to-thickness ratio, CNT volume fraction, plate aspect ratio, in-plane loading condition, boundary condition and temperature change on buckling load parameter $\overline{N}_{cr} = N_{cr} b^2 / E_m h^3$ of various types of CNTRC plates (see Table 3).

Buckling load parameters are as in Tables 4–6 for various types of CNTRC plates subjected to uniaxial compression ($\gamma_1 = -1$, $\gamma_2 = 0$), biaxial compression ($\gamma_1 = -1$, $\gamma_2 = -1$) and biaxial compression and tension ($\gamma_1 = -1$, $\gamma_2 = 1$) with different boundary conditions. Width-to-thickness ratio of the plates is set to be $b/h = 10$ and CNT volume fraction is taken to be $V_{CNT}^* = 0.11$. In each table, three types of CNTRC plates and six different boundary conditions are considered. The boundary conditions are given as follows:

Simply supported (S) : At $x = 0$, $\quad a : v_0 = w_0 = \phi_y = 0$,
At $y = 0$, $\quad b : u_0 = w_0 = \phi_x = 0$.
Clamped (C) : At $x = 0$, $\quad a : v_0 = w_0 = \phi_x = \phi_y = 0$,
At $y = 0$, $\quad b : u_0 = w_0 = \phi_x = \phi_y = 0$.

Table 1
Comparison of Young's moduli for PmPV/CNT composites reinforced by (10, 10) SWCNT under $T = 300$ K.

V_{CNT}^*	MD [7]		Rule of mixture			
	E_{11} (GPa)	E_{22} (GPa)	E_{11} (GPa)	η_1	E_{22} (GPa)	η_2
0.11	94.8	2.2	94.57	0.149	2.2	0.934
0.14	120.2	2.3	120.09	0.150	2.3	0.941
0.17	145.6	3.5	145.08	0.149	3.5	1.381

Table 2
Buckling load parameter $\overline{N}_{cr} = N_{cr}a^2/D_0$ for simply supported isotropic plate under uniaxial compressive pressure ($\gamma_1 = -1$, $\gamma_2 = 0$).

Mode	Present					Analytical [42]
	13×13	15×15	17×17	19×19	21×21	
1	39.4717	39.3541	39.2327	39.1898	39.1744	39.4761
2	59.5340	59.9442	60.2003	60.3336	60.4874	61.6814
3	100.628	102.703	103.810	104.739	105.391	109.656
4	146.802	149.578	150.867	151.558	152.501	157.904

Table 3
Effect of boundary conditions on buckling load parameter $\overline{N}_{cr} = N_{cr}b^2/E_mh^3$ for various types of CNTRC plates under uniaxial compression ($\gamma_1 = -1$, $\gamma_2 = 0$).

Mode	Boundary conditions					
	SSSS	CCCC	SCSC	SFSF	CCCF	SSSF
UD						
1	14.1073	25.7329	17.2424	12.0697	22.6030	12.3145
2	23.3149	26.2788	24.0481	13.0216	24.8135	16.6801
3	25.6506	29.6661	26.0993	20.3912	26.4696	22.5393
4	27.0498	29.7356	27.4953	22.4198	26.9602	24.1999
FG-O						
1	9.8306	21.1221	12.9407	7.5979	17.7447	7.8954
2	18.6106	22.8513	19.3502	8.7307	21.3317	12.5971
3	23.0443	27.4064	23.9445	16.5875	22.1059	17.7061
4	23.5067	27.7713	24.4292	17.5352	23.6396	19.7792
FG-X						
1	17.0631	27.8882	20.2230	15.1414	24.9924	15.3520
2	25.6219	27.9271	26.3162	15.9786	26.4526	19.5212
3	26.6656	30.4525	27.0017	23.0097	28.5261	24.9021
4	28.6004	30.6129	28.9246	24.8098	28.5546	25.9519

Table 4
Effect of boundary conditions on buckling load parameter $\overline{N}_{cr} = N_{cr}b^2/E_mh^3$ for various types of CNTRC plates under biaxial compression ($\gamma_1 = -1$, $\gamma_2 = -1$).

Mode	Boundary conditions					
	SSSS	CCCC	SCSC	SFSF	CCCF	SSSF
UD						
1	5.8831	9.2830	7.4017	3.1893	8.1646	3.4105
2	6.9772	9.8992	7.7597	3.7162	9.1245	6.0466
3	7.8892	13.1796	10.8992	7.1140	9.8911	7.8034
4	10.6318	13.5820	13.0521	7.7648	11.2443	7.9533
FG-O						
1	4.8946	8.6006	5.7889	2.6628	7.7420	2.8174
2	5.1057	9.0925	7.0471	3.0824	8.2474	5.0733
3	7.4827	12.0069	10.1848	5.4130	9.3315	6.3872
4	10.3448	13.1827	12.2440	7.2015	10.8971	7.2482
FG-X						
1	6.4384	9.6510	8.2764	3.5390	8.3985	3.7579
2	8.1924	10.2682	8.3625	4.0248	9.5378	6.7678
3	8.4092	13.7356	11.5431	8.0983	10.2331	8.1427
4	10.8848	13.8683	13.3630	8.2506	11.4406	8.2934

Table 5
Effect of boundary conditions on buckling load parameter $\overline{N}_{cr} = N_{cr}b^2/E_mh^3$ for various types of CNTRC plates under biaxial compression and tension ($\gamma_1 = -1$, $\gamma_2 = 1$).

Mode	Boundary conditions					
	SSSS	CCCC	SCSC	SFSF	CCCF	SSSF
UD						
1	28.4768	31.1006	28.5901	22.4705	26.4640	24.0547
2	28.8410	31.2469	29.1082	26.7125	26.5452	27.5122
3	29.5768	31.2907	29.6525	28.3144	29.6448	28.6198
4	30.1219	31.3367	30.1596	28.5690	29.8224	29.0144
FG-O						
1	24.0474	27.9340	25.0796	17.5847	21.4325	18.9241
2	26.1762	28.1397	26.5121	23.2046	22.7898	23.9607
3	27.7905	29.7081	27.9939	24.1482	27.5293	26.5443
4	28.0947	29.9150	28.2740	26.0577	27.6694	27.4088
FG-X						
1	29.1897	31.3870	29.2382	24.8624	28.3064	26.5559
2	29.8851	31.5879	29.9561	28.1899	28.5949	28.9456
3	30.2610	31.6207	30.3072	28.8976	30.4639	29.1912
4	30.6195	31.6568	30.6433	29.5367	30.6519	29.9469

Table 6
Effect of temperature on buckling load parameter $\overline{N}_{cr} = N_{cr}b^2/E_mh^3$ for various types of CNTRC plates under uniaxial compression ($\gamma_1 = -1$, $\gamma_2 = 0$).

Mode	Type of CNTRC		
	UD	FG-O	FG-X
300			
1	30.9076	18.7534	40.8005
2	46.9779	34.4733	57.3978
3	69.3855	48.4971	82.0077
4	74.5610	54.0994	86.8162
500			
1	24.9500	15.6500	31.7259
2	33.4917	24.0892	40.4903
3	47.8115	36.3066	52.5178
4	50.0545	39.0459	54.1447
700			
1	9.9080	7.8312	10.9229
2	11.0824	9.2321	11.6558
3	11.5691	10.4122	12.5167
4	12.4589	11.4780	12.8683

It is observed that for six different boundary conditions, plates with four fully clamped edges (CCCC) have the maximum buckling load values, whereas the plates with two edges simply supported and two edges free (SFSF) have the minimum buckling load values since constraints of boundary conditions become weaker with the order of clamped (C), simply supported (S) and free (F) edges.

Figs. 2–4 show the variation of buckling load parameters of various types of simply supported square CNTRC plates under different loading conditions versus CNT volume fraction. The results show that buckling load parameter of the plates has a higher value when the volume fraction of CNT is larger since the stiffness of CNTRC plates is larger when the value of CNT volume fraction is higher. Moreover, for all different distributions of CNTs, FG-X plates have larger buckling load values than UD plates and values of FG-O plates are smaller than UD plates. That is expected since CNT reinforcements distributed close to top and bottom are more efficient than those distributed near the mid-plane for increasing the stiffness of CNTRC plates [16].

Figs. 5–7 show the variation of buckling load parameters of various types of simply supported square CNTRC plates under different loading conditions versus plate width-to-thickness ratio. CNT volume fractions of the plates are taken to be $V^*_{CNT} = 0.11$. It can be seen that as the width-to-thickness ratio of the plate increases, the non-dimensional buckling load parameters increase and buckling load parameters for UN-CNTRC plates and the other two types of FG-CNTRC plates increase more slowly. The results also show that effect of distribution of CNTs becomes weaker for moderately thick CNTRC plates, as shown in Fig. 7.

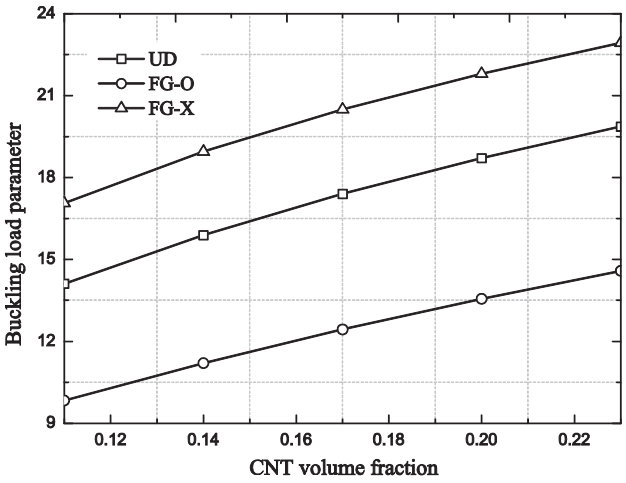

Fig. 2. Variation of the buckling load parameter of simply supported various types of CNTRC plates versus the CNT volume fraction under uniaxial compression ($\gamma_1 = -1$, $\gamma_2 = 0$).

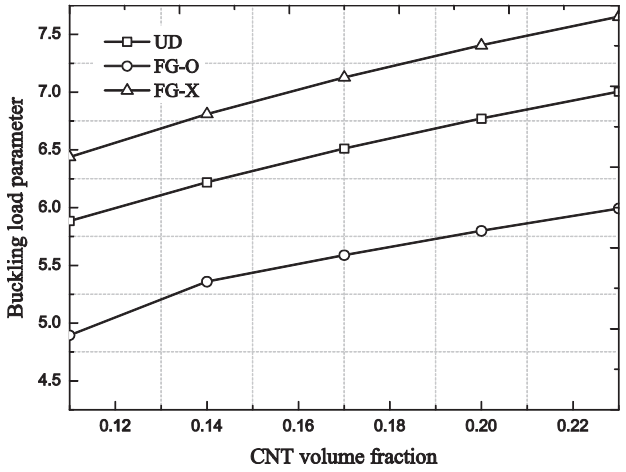

Fig. 3. Variation of the buckling load parameter of simply supported various types of CNTRC plates versus the CNT volume fraction under biaxial compression ($\gamma_1 = -1$, $\gamma_2 = -1$).

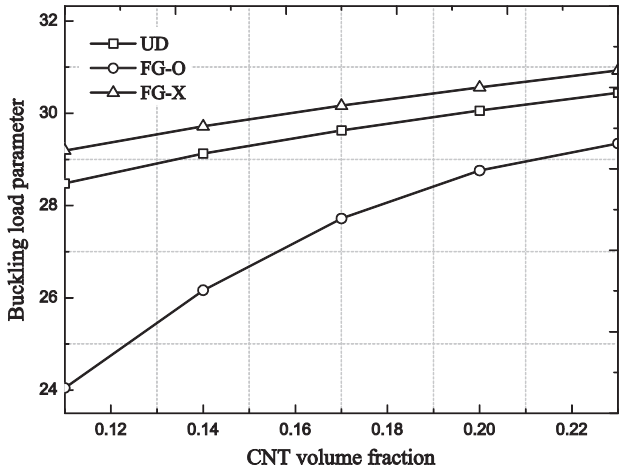

Fig. 4. Variation of the buckling load parameter of simply supported various types of CNTRC plates versus the CNT volume fraction under biaxial compression and tension ($\gamma_1 = -1$, $\gamma_2 = 1$).

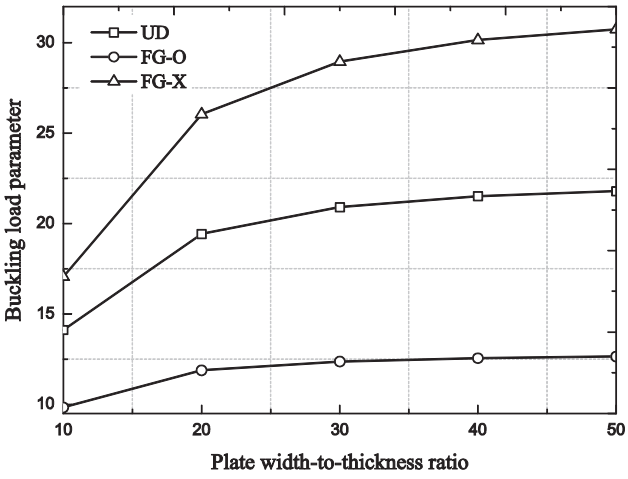

Fig. 5. Variation of the buckling load parameter of simply supported various types of CNTRC plates versus the plate width-to-thickness ratio under uniaxial compression ($\gamma_1 = -1$, $\gamma_2 = 0$).

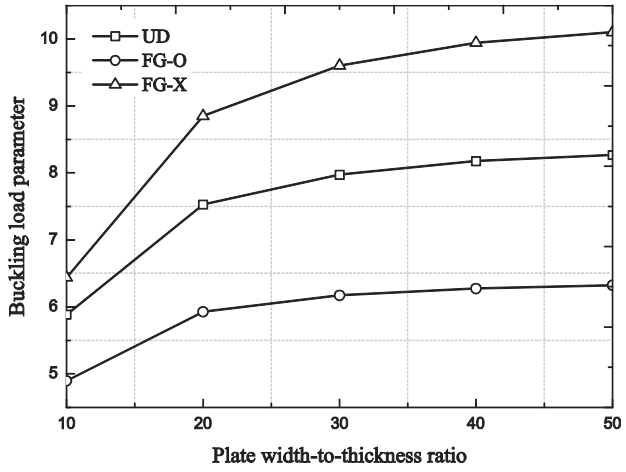

Fig. 6. Variation of the buckling load parameter of simply supported various types of CNTRC plates versus the plate width-to-thickness ratio under biaxial compression ($\gamma_1 = -1$, $\gamma_2 = -1$).

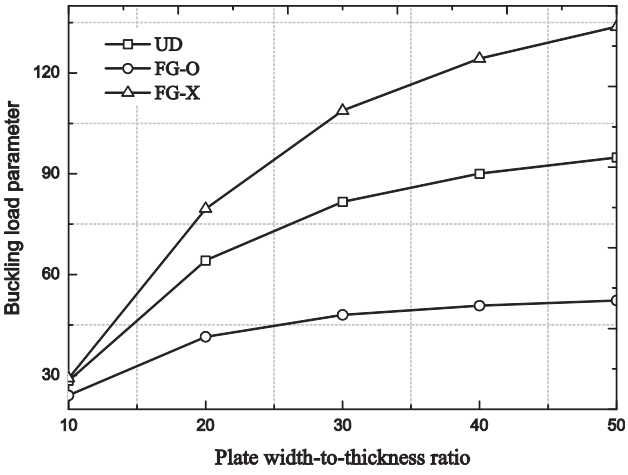

Fig. 7. Variation of the buckling load parameter of simply supported various types of CNTRC plates versus the plate width-to-thickness ratio under biaxial compression and tension ($\gamma_1 = -1$, $\gamma_2 = 1$).

Figs. 8–10 show buckling load parameters for simply supported square UD- and the other two types of FG-CNTRC plates with plate aspect ratio ($\beta = a/b$) changing from 1.0 to 2.0. The plate width-to-thickness ratio (b/h) is set to be 20. It can be seen that buckling load parameters decrease as plate aspect ratio changes from 1.0 to 2.0. It is worth noting that the change of plate aspect ratio has a very small effect on buckling load parameter for CNTRC plates under biaxial compression and tension ($\gamma_1 = -1$, $\gamma_2 = 1$), as shown in Fig. 10.

Effects of temperature change ($T = 300$, 500 and 700 K) on buckling load parameters of simply supported square CNTRC plates of various types under different loading conditions are shown in Tables 6–8. For this study, the extended rule of mixture is used to predict effective material properties of CNTRCs. As shown in Table 1, Young's moduli E_{11} and E_{22} of CNTRCs (obtained by the rule of mixture) match very well with molecular simulation results [7]. Width-to-thickness ratio (b/h) of the plates is set to be 20 and CNT volume fraction V^*_{CNT} is taken to be 0.11. It can be seen that buckling load parameters decrease as temperature increases because with increase of temperature, elastic moduli of CNTRC plates are reduced and stiffness of nanocomposites becomes weaker since

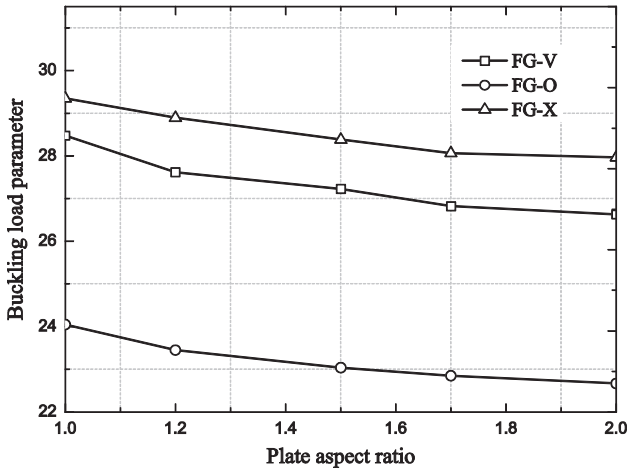

Fig. 10. Variation of the buckling load parameter of simply supported various types of CNTRC plates versus plate aspect ratio under biaxial compression and tension ($\gamma_1 = -1$, $\gamma_2 = 1$).

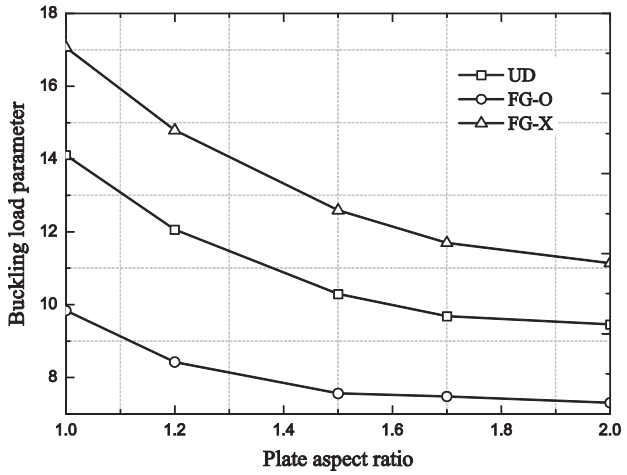

Fig. 8. Variation of the buckling load parameter of simply supported various types of CNTRC plates versus plate aspect ratio under uniaxial compression ($\gamma_1 = -1$, $\gamma_2 = 0$).

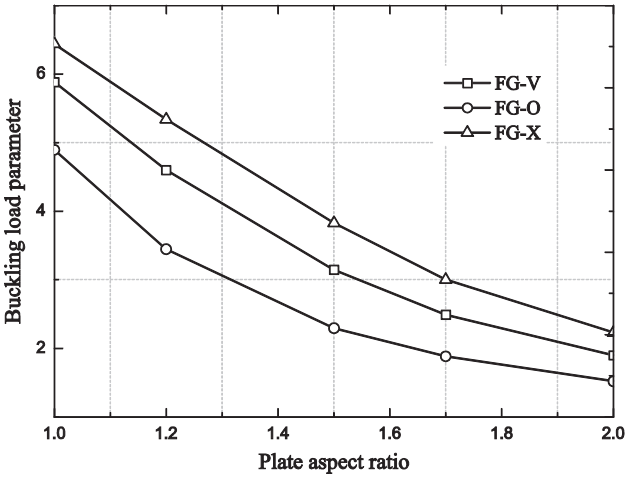

Fig. 9. Variation of the buckling load parameter of simply supported various types of CNTRC plates versus plate aspect ratio under biaxial compression ($\gamma_1 = -1$, $\gamma_2 = -1$).

Table 7
Effect of temperature on buckling load parameter $\overline{N}_{cr} = N_{cr}b^2/E_m h^3$ for various types of CNTRC plates under biaxial compression ($\gamma_1 = -1$, $\gamma_2 = -1$).

Mode	Type of CNTRC		
	UD	FG-O	FG-X
300			
1	9.3805	6.9161	11.4231
2	10.3981	8.9197	11.6524
3	14.0470	9.3380	15.0540
4	15.3108	12.7496	19.6846
500			
1	6.4261	4.8122	7.2278
2	6.6468	5.3809	7.9999
3	8.1205	7.2727	8.7376
4	10.6318	7.7577	11.1593
700			
1	1.6662	1.4421	1.7938
2	1.7822	1.6040	1.8869
3	2.1605	1.8075	2.2538
4	2.1979	1.9780	2.3949

Table 8
Effect of temperature on buckling load parameter $\overline{N}_{cr} = N_{cr}b^2/E_m h^3$ for various types of CNTRC plates under biaxial compression and tension ($\gamma_1 = -1$, $\gamma_2 = 1$).

Mode	Type of CNTRC		
	UD	FG-O	FG-X
300			
1	89.9909	63.4215	104.9802
2	101.0670	81.0655	108.9411
3	107.7075	92.2314	113.8593
4	109.0635	95.2431	117.1884
500			
1	60.3588	47.1796	63.0943
2	61.4624	54.2048	65.6711
3	63.9377	58.2656	66.7473
4	65.8997	58.6951	67.8585
700			
1	12.7391	12.3343	12.9951
2	13.1208	12.8971	13.2835
3	13.2501	13.0608	13.4060
4	13.3643	13.1740	13.5197

material properties of the matrix and SWCNTs are assumed to be temperature-dependent. We also found that FG-X and FG-O CNTRC plates have the highest and lowest values of buckling load parameters, respectively, in different temperature environments.

5. Conclusion

In this paper, the element-free *kp*-Ritz method is successfully applied to buckling analysis of CNTRC plates. The plates are reinforced by SWCNTs and effective material properties of CNTRC plates are estimated either by the Eshelby–Mori–Tanaka approach or the extended rule of mixture. The first-order shear deformation theory is employed and a kernel particle estimate is used to approximate the two-dimensional displacement field. Comparison studies were performed to verify the accuracy and efficiency of the present method and the results were found to be in good agreement with solutions available in literature. Detailed case studies are conducted and it is concluded that the change of CNT volume fraction, plate width-to-thickness ratio, plate aspect ratio, temperature, boundary conditions and loading conditions have pronounced effects on buckling strength of various types of CNTRC plates. Moreover, it is noteworthy that distribution type of CNT also significantly affects buckling strength of CNTRC plates.

References

[1] Esawi AMK, Farag MM. Carbon nanotube reinforced composites: potential and current challenges. Mater Des 2007;28:2394–401.
[2] Lau AKT, Hui D. The revolutionary creation of new advanced materials—carbon nanotube composites. Composites: Part B 2002;33:263–77.
[3] Thostenson ET, Ren Z, Chou TW. Advances in the science and technology of carbon nanotubes and their composites: a review. Compos Sci Technol 2001;61:1899–912.
[4] Odegard GM, Gates TS, Wise KE, Park C, Siochi EJ. Constitutive modeling of nanotube–reinforced polymer composites. Compos Sci Technol 2003;63:1671–87.
[5] Seidel GD, Lagoudas DC. Micromechanical analysis of the effective elastic properties of carbon nanotube reinforced composites. Mech Mater 2006;38:884–907.
[6] Fidelus JD, Wiesel E, Gojny FH, Schulte K, Wagner HD. Thermo-mechanical properties of randomly oriented carbon/epoxy nanocomposites. Composites: Part A 2005;36:1555–61.
[7] Han Y, Elliott J. Molecular dynamics simulations of the elastic properties of polymer/carbon nanotube composites. Comput Mater Sci 2007;39:315–23.
[8] Zhu R, Pan E, Roy AK. Molecular dynamics study of the stress–strain behavior of carbon-nanotube reinforced Epon 862 composites. Mater Sci Eng, A 2007;447:51–7.
[9] Wuite J, Adali S. Deflection and stress behaviour of nanocomposite reinforced beams using a multiscale analysis. Compos Struct 2005;71:388–96.
[10] Vodenitcharova T, Zhang LC. Bending and local buckling of a nanocomposite beam reinforced by a single-walled carbon nanotube. Int J Solids Struct 2006;43:3006–24.
[11] Formica G, Lacarbonara W, Alessi R. Vibrations of carbon nanotube-reinforced composites. J Sound Vib 2010;329:1875–89.
[12] Arani A, Maghamikia S, Mohammadimehr M, Arefmanesh A. Buckling analysis of laminated composite rectangular plates reinforced by SWCNTs using analytical and finite element methods. J Mech Sci Technol 2011;25:809–20.
[13] Shen HS. Postbuckling of nanotube-reinforced composite cylindrical shells in thermal environments. Part I: Axially-loaded shells. Compos Struct 2011;93:2096–108.
[14] Shen HS. Postbuckling of nanotube-reinforced composite cylindrical shells in thermal environments. Part II: Pressure-loaded shells. Compos Struct 2011;93:2496–503.
[15] Shen HS. Nonlinear bending of functionally graded carbon nanotube-reinforced composite plates in thermal environments. Compos Struct 2009;91:9–19.
[16] Zhu P, Lei ZX, Liew KM. Static and free vibration analyses of carbon nanotube-reinforced composite plates using finite element method with first order shear deformation plate theory. Compos Struct 2012;94:1450–60.
[17] Ke LL, Yang J, Kitipornchai S. Nonlinear free vibration of functionally graded carbon nanotube-reinforced composite beams. Compos Struct 2010;92:676–83.
[18] Shen HS, Zhang CL. Thermal buckling and postbuckling behavior of functionally graded carbon nanotube-reinforced composite plates. Mater Des 2010;31:3403–11.
[19] Zhao X, Li Q, Liew KM, Ng TY. The element-free-Ritz method for free vibration analysis of conical shell panels. J Sound Vib 2006;295:906–22.
[20] Liew KM, Wang J, Tan MJ, Rajendran S. Postbuckling analysis of laminated composite plates using the mesh-free kp-Ritz method. Comput Methods Appl Mech Eng 2006;195:551–70.
[21] Zhao X, Liew KM, Ng TY. Vibration analysis of laminated composite cylindrical panels via a meshfree approach. Int J Solids Struct 2003;40:161–80.
[22] Liew KM, Ng TY, Zhao X, Reddy JN. Harmonic reproducing kernel particle method for free vibration analysis of rotating cylindrical shells. Comput Methods Appl Mech Eng 2002;191:4141–57.
[23] Chang TC, Geng JY, Guo XM. Chirality- and size-dependent elastic properties of single-walled carbon nanotubes. Appl Phys Lett 2005;87.
[24] Elliott JA, Sandler JKW, Windle AH, Young RJ, Shaffer MSP. Collapse of single-wall carbon nanotubes is diameter dependent. Phys Rev Lett 2004;92:095501.
[25] Jin Y, Yuan FG. Simulation of elastic properties of single-walled carbon nanotubes. Compos Sci Technol 2003;63:1507–15.
[26] Liew KM, Yan JW, Sun YZ, He LH. Investigation of temperature effect on the mechanical properties of single-walled carbon nanotubes. Compos Struct 2011;93:2208–12.
[27] Li X, Gao H, Scrivens WA, Fei D, Xu X, Sutton MA, et al. Reinforcing mechanisms of single-walled carbon nanotube-reinforced polymer composites. J Nanosci Nanotechnol 2007;7:2309–17.
[28] Seidel GD, Lagoudas DC. Micromechanical analysis of the effective elastic properties of carbon nanotube reinforced composites. Mech Mater 2006;38:884–907.
[29] Librescu L, Oh S-Y, Song O. Thin-walled beams made of functionally graded materials and operating in a high temperature environment: vibration and stability. J Therm Stress 2005;28:649–712.
[30] Aragh BS, Barati AHN, Hedayati H. Eshelby–Mori–Tanaka approach for vibrational behavior of continuously graded carbon nanotube-reinforced cylindrical panels. Composites: Part B 2012;43:1943–54.
[31] Eshelby JD. The determination of the elastic field of an ellipsoidal inclusion, and related problems. Proc Roy Soc Lond, Ser A 1957;241:376–96.
[32] Eshelby JD. The elastic field outside an ellipsoidal inclusion. Proc Roy Soc Lond, Ser A 1959;252:561–9.
[33] Mori T, Tanaka K. Average stress in matrix and average elastic energy of materials with misfitting inclusions. Acta Metall 1973;21:571–4.
[34] Benveniste Y. A new approach to the application of Mori–Tanaka's theory in composite materials. Mech Mater 1987;6:147–57.
[35] Mura T. Micromechanics of defects in solids. Second ed. The Netherlands: Martinus Nijhoff; 1987.
[36] Reddy JN. Mechanics of laminated composite plates and shells: theory and analysis. Second ed. Boca Raton, FL: CRC Press; 2004.
[37] Efraim E, Eisenberger M. Exact vibration analysis of variable thickness thick annular isotropic and FGM plates. J Sound Vib 2007;299:720–38.
[38] Chen JS, Pan C, Wu CT, Liu WK. Reproducing kernel particle methods for large deformation analysis of non-linear structures. Comput Methods Appl Mech Eng 1996;139:195–227.
[39] Chen JS, Wu CT, Yoon S, You Y. A stabilized conforming nodal integration for Galerkin mesh-free methods. Int J Numer Methods Eng 2001;50:435–66.
[40] Beissel S, Belytschko T. Nodal integration of the element-free Galerkin method. Comput Methods Appl Mech Eng 1996;139:49–74.
[41] Popov VN, Doren VEV, Balkanski M. Elastic properties of crystals of single-walled carbon nanotubes. Solid State Commun 2000;114:395–9.
[42] Timoshenko S, Gere J. Theory of elastic stability. 2nd ed. New York: McGraw-Hill; 1961.